Pulsar Timing for the GLAST Large Area Telescope

D. A. Smith[1], L. Guillemot[1], F. Camilo[2], I. Cognard[3], D. Dumora[1], C. Espinoza[4], P. C. C. Freire[5], E. V. Gotthelf[2], A. K. Harding[6], G. B. Hobbs[7], S. Johnston[7], M. Kramer[4], M. A. Livingstone[8], A. G. Lyne[4], R. N. Manchester[7], F. E. Marshall[6], M. A. McLaughlin[9], A. Noutsos[4], S. M. Ransom[10], M. S. E. Roberts[11], R. W. Romani[12], G. Theureau[3], D. J. Thompson[6], S. E. Thorsett[13], N. Wang[14], and P. Weltevrede[7]

[1] Centre d'études nucléaires de Bordeaux Gradignan - CENBG UMR 5797 CNRS/IN2P3 - Université Bordeaux 1, Chemin du Solarium - BP120 33175 Gradignan cedex, France
[2] Columbia Astrophysics Laboratory, Columbia University, New York, NY 10027, USA
[3] Laboratoire de Physique et Chimie de l'Environnement, LPCE UMR 6115 CNRS, 45071 Orléans cedex 02, France
Station de radioastronomie de Nançay, Observatoire de Paris, CNRS/INSU, 18330 Nançay, France
[4] University of Manchester, Jodrell Bank Observatory, Macclesfield, Cheshire SK11 9DL, UK
[5] Arecibo Observatory, HC 3 Box 53995, Arecibo, Puerto Rico 00612, USA
[6] NASA Goddard Space Flight Center, Greenbelt, MD 20771, USA
[7] Australia Telescope National Facility, CSIRO, PO Box 76, Epping NSW 1710, Australia
[8] McGill University, Montreal, Quebec, Canada
[9] West Virginia University, Department of Physics, PO Box 6315, Morgantown, WV 26506, USA
[10] National Radio Astronomy Observatory, Charlottesville, VA 22903, USA
[11] Eureka Scientific, Inc., 2452 Delmer Street Suite 100, Oakland, CA 94602-3017, USA
[12] Department of Physics, Stanford University, California, USA
[13] Department of Astronomy & Astrophysics, University of California, Santa Cruz, CA 95064, USA
[14] National Astronomical Observatories-CAS, 40-5 South Beijing Road, Urumqi 830011, China

ABSTRACT

We describe a comprehensive pulsar monitoring campaign for the Large Area Telescope (LAT) on the Gamma Large Area Telescope (GLAST). LAT's unprecedented sensitivity between 20 MeV and 300 GeV together with its 2.4 sr field-of-view justifies the monitoring of over two hundred pulsars with large spindown powers. To search for gamma-ray pulsations from these pulsars requires a set of phase-connected timing solutions spanning a year or more to properly align the sparse photon arrival times. We describe the choice of pulsars, and the instruments involved in the campaign. Attention is paid to verifications of the LAT pulsar software, using for example giant radio pulses from the Crab and from PSR B1937+21 recorded at Nançay, and using X-ray data on PSR J0218+4232 from XMM-Newton. We demonstrate accuracy of the pulsar phase calculations at the microsecond level.

Key words. pulsars:general – Gamma rays:observations – Ephemerides

1. Introduction

Forty years after the discovery of rotating neutron stars much is unknown about their emission processes, and in particular the radio emission mechanism is still largely not understood (Lorimer & Kramer 2004). Of the nearly two thousand known pulsars, six have been detected in GeV gamma rays with high confidence, using the EGRET detector on the *Compton Gamma Ray Observatory* (CGRO) (Thompson et al. 1999).

The Large Area Telescope (LAT) on the *Gamma Large Area Space Telescope* satellite (GLAST) will go into orbit in 2008 (Michelson et al. 2008). The sensitivity and time resolution of this instrument will allow it to discover tens or more of new gamma-ray pulsars (Smith & Thompson 2008). Notably, it will be able to determine the sources among the 169 unidentified EGRET sources that are pulsars. However, even with a sensitivity more than 30 times greater than that of EGRET, and even more at high energy, the LAT's rate of gamma-ray photon detection will be small. For example, the Crab pulsar is the third brightest known gamma-ray pulsar, but will trigger the LAT only

once every 500 revolutions of the neutron star (15 seconds), on average. While the Crab pulsar should be detected by the LAT with high confidence in less than a day, it will take years to detect pulsars near the sensitivity threshold, with days separating individual photon arrival times. A search for pulsations using gamma-ray data alone is exceedingly difficult in these conditions, if not impossible (Atwood et al. 2006; Ransom 2007). Accurate knowledge of the rotation parameters increases LAT pulsed sensitivity. However, many neutron stars slow down irregularly, a phenomenon known as "timing noise", making it difficult to extrapolate a pulsar's rotation frequency ν from one epoch to another. Consequently, in order to obtain the accurate ephemerides necessary for gamma-ray detection of pulsations, known pulsars must be observed regularly. In anticipation of GLAST launch, and mindful of the requirement for accurate, contemporaneous timing parameters in order to observe pulsars at gamma-ray energies, we began an extensive campaign of pulsar timing observations with the Parkes 64-meter radio telescope in Australia, with the Lovell 76-meter telescope at the Jodrell Bank observatory near Manchester, England, and with the 94-meter (equivalent) Nançay radio telescope near Orleans, France.

These observatories carry out observing programs in support of the GLAST mission and, between them, observe more than 200 pulsars with a large spin-down, $\dot{E} = \frac{dE}{dt}$, as described below, on a regular basis. In addition, about a dozen pulsars with weak radio emission that are particularly strong candidates for gamma-ray emission are being observed periodically with the Green Bank radio telescope (GBT) and the Arecibo radio telescope. Four pulsars with no detectable radio emission are being observed with the Rossi X-ray Timing Explorer satellite (RXTE). The goal is to build a database of rotation parameters that will allow folding of the gamma rays as they are accumulated over the 5 to 10 year GLAST mission duration. This work is similar in spirit to what was done for CGRO (Arzoumanian et al. 1994; D'Amico et al. 1996; Johnston et al. 1995).

2. Pulsars and the Large Area Telescope

The LAT is described in Michelson et al. (2008). In brief, most gamma rays convert to electron-positron pairs in tungsten foil interleaved with the 32 layers of silicon microstrip detectors in the tracker, yielding direction information. The particle cascade continues in the cesium iodide crystals of the calorimeter, providing energy information. Scintillators surrounding the tracker aid rejection of the charged cosmic ray background. The scintillators are segmented to reduce the "backsplash": a self-veto effect that reduced EGRET's sensitivity to high energy photons.

Gamma-ray events recorded with the LAT have timestamps that derive from a GPS clock on the GLAST satellite. The mission requirement is for ± 10 μs absolute time precision, with a goal to achieve ± 2 μs, when signals from the GPS satellite constellation are being processed. When GPS lock is lost, the absolute timing is required to drift by no more than 1 μs per 100 seconds. Results from ground tests showed accuracy surpassing the goals (Smith et al. 2008), and on-orbit performance is expected to be comparable.

The LAT is a 4-by-4 array of detector "modules" covering an area of roughly 1.7 meters on a side. It is sensitive to photons with energies between 20 MeV and 300 GeV, whereas EGRET's sensitivity fell off significantly above 10 GeV. After event reconstruction and background rejection, the effective area for gamma rays above 1 GeV is 8000 cm^2 at normal incidence, as compared to 1200 cm^2 for EGRET. The angular resolution is also better than EGRET's, such that source localisation for typical sources will be of order of $0.1°$[1]. The height-to-width aspect ratio of the LAT is 0.4, for a field-of-view of over 2 sr, or nearly 20% of the sky at a given time. Combined with the large effective area, this makes a sky survey observation strategy possible: on a given orbit, the LAT will sweep the sky 35° away from the orbital plane, covering 75% of the sky. At the end of the orbit, GLAST will rock to 35° on the other side of the orbital plane, and continue to scan. Thus, the entire sky is covered with good uniformity every three hours, and no time is lost to earth occultation. Survey mode, large effective area, and good localisation together give the LAT an overall steady point-source sensitivity 30 times better than EGRET's.

The EGRET pulsars showed a variety of pulse profiles and emission spectra and raised as many questions as they answered (Thompson et al. 1999). The high-energy emission is thought to arise from basic electromagnetic interactions of highly relativistic particles, namely synchrotron emission, curvature emission

---

[1] Details of the instrument response are maintained at http://www-glast.slac.stanford.edu/software/IS/glast_lat_performance.htm

and inverse Compton emission. Gamma-ray observations of pulsars provide a direct probe of particle acceleration and signatures of non-thermal phenomena taking place in their magnetospheres (Harding 2007), and may also provide clues to the fundamental physics responsible for the elusive radio emission mechanism. There are two main categories of models describing the properties of high-energy emission of pulsars. In both cases, charged particles are accelerated along the magnetic dipole field lines by parallel electric fields. The main difference between these two families is the particle acceleration region. The Polar Cap model (Ruderman & Sutherland 1975; Sturrock 1971) argues that the acceleration begins above the stellar magnetic pole, but can extend to the outer magnetosphere. In the Outer Gap model (Cheng et al. 1986a,b) particles are thought to be accelerated to high energies only in the outer magnetosphere, in vacuum gaps between a null-charge surface and the light cylinder. The Polar Cap and the Outer Gap models predict different high-energy emission features such as spectra and profiles, that LAT observations may elucidate, through a hierarchy of observables. First, the different models have very different predictions of which and how many pulsars emit gamma rays. Along with detections of radio-quiet pulsars in gamma rays using blind search techniques, this will constrain the ratio of radio-loud to radio-quiet pulsars. This ratio is different for the two emission models, with outer gap models predicting a much lower ratio (Gonthier et al. 2004; Harding et al. 2007). Reliable flux upper limits in the absence of gamma-ray pulsations are useful in this context (Nel et al. 1996) and also require good timing solutions.

The second observable is the emission profile. Its shape, as the beam sweeps the Earth, provides a cross-section of the regions in the pulsar magnetosphere where the emission originates. Coupled with radio intensity and polarization profile studies, as well as absolute phase, the gamma-ray light curve provides information on the emission geometry, which differs significantly from one model to another (Chiang & Romani 1994; Gonthier et al. 2002). The EGRET pulsars typically have two peaks, with the first one slightly offset in phase relative to the single radio peak. Although the Crab pulsar breaks this trend, LAT observations will show the prevalence of this behaviour as a function of pulsar age or other parameters. Pulsar detections and emission profiles can only be achieved through solid knowledge of the pulsar's rotation and good absolute time precision. The timing precision will allow finely binned profiles for fast pulsars like PSR J0218+4232 over many years, assuming that the gamma-ray flux of this millisecond pulsar is as stated in Kuiper et al. (2004).

Finally, the large energy range covered by the LAT will enable measurements of pulsar spectral cut-offs. Although EGRET observed high-energy cut-offs in pulsar spectra around a few GeV, it did not have the sensitivity to measure the exact energy or shape of the turnovers. For instance, the LAT should provide a determination of the Crab pulsar's spectral cut-off energy, known only to be less than a few tens of GeV (Albert et al. 2008; de Naurois et al. 2002), where EGRET lost sensitivity due to the backsplash effect. Spectral cut-offs are powerful discriminators. The on-axis energy resolution is better than 15% above 100 MeV and is better than 10% in the range between roughly 500 MeV and 50 GeV, and improves somewhat off-axis. The LAT should be able to measure the shape of the Vela pulsar spectral cut-off expected to be around 4 GeV, a powerful discriminator between Polar Cap and Outer Gap models and a potential diagnostic of high-energy emission altitude (Harding 2007). This will lead to a better comprehension of particle emission mechanisms in the pulsar magnetosphere. Finally, a subset of the

pulsars detected by the LAT will have high enough statistics to allow phase-resolved spectroscopy, offering further insight into emission mechanisms and the beam geometry.

GLAST will monitor all pulsars continuously with a duty-cycle of roughly one-third, because of its survey mode, unlike EGRET or the *Astro-rivelatore Gamma a Immagini LEggero* (AGILE) telescope (Pellizzoni et al. 2004), which went into orbit in April, 2007. A drawback of the survey strategy is that having the sample of gamma photons spread over a longer duration makes phase-folding more difficult, as long-term timing noise may appear in pulsar spin behavior and glitches may occur (Ransom 2007). The need for a substantial and sustained pulsar timing campaign stems in part from this continuous observation, whereas pointing telescopes only require monitoring during observations of any given sky region.

3. The Timing Campaign

3.1. Gamma-Ray pulsar candidates

For a pulsar with a rotation frequency ν, in Hz, and frequency derivative $\dot{\nu}$, the spin-down power is $\dot{E} = -4\pi^2 I \nu \dot{\nu}$ erg/s where the moment of inertia I is taken to be 10^{45} g cm^2, ν is expressed in Hz and $\dot{\nu} = \frac{d\nu}{dt}$ in units of Hz^2. The open field-line voltage is $V \simeq 6.3 \times 10^{20} \sqrt{-\nu\dot{\nu}} \simeq 3.18 \times 10^{-3} \sqrt{\dot{E}}$ volts. Above some value of V, or, equivalently, $\dot{E}$, gamma-ray emitting electron-positron cascades occur, with gamma-ray luminosity L_γ increasing with $\dot{E}$ (Arons 1996). A linear dependence of L_γ on V would give $L_\gamma \propto \nu^{0.5}\dot{\nu}^{0.5} \propto \sqrt{\dot{E}}$, leading to a gamma-ray production efficiency $\epsilon_\gamma = L_\gamma/\dot{E} \propto 1/\sqrt{\dot{E}}$. Analyses based on EGRET pulsar detections and upper limits have constrained gamma-ray luminosity laws (e.g. McLaughlin & Cordes 2000), an update of which yields $L_\gamma \propto \sim \nu^{-0.9}\dot{\nu}^{0.6}$. Empirically, although based on a small handful of gamma-ray pulsars, the minimum spindown threshold seems to be near $\dot{E} \simeq 3 \times 10^{34}$ erg/s (Thompson et al. 1999). The angular size and viewing geometry of pulsar beams is difficult to constrain and introduces a large uncertainty in the relation between a minimum $\dot{E}$ and the expected gamma-ray flux. Bright radio pulsars may have gamma-ray beams missing the Earth's line-of-sight; conversely at least one bright gamma-ray pulsar, Geminga, has no detectable radio flux (Burderi et al. 1999). Balancing these issues, and keeping the list of gamma-ray pulsar candidates of reasonable length, we have selected pulsars with

$$\dot{E} > 10^{34} \text{ erg/s}$$

for GLAST pulsar timing. From the ATNF online catalogue (Manchester et al. 2005) we obtain 230 such pulsars. We give lower priority to the timing of the pulsars in globular clusters since they can have apparent $\dot{E}$ values higher than the true spin-down power of the neutron star, due to acceleration in the gravitational potential of the cluster. This leaves us with **224 pulsars** which we believe are imperative to time regularly.

Table 1 gives the pulsar names as well as some indicators of whether they may be gamma-ray emitters, such as $\dot{E}$ and associations with other high-energy sources[2]. The distance d (the variable "DIST1") is taken from the ATNF database. It is based on the NE2001 model for the Galactic distribution of free electrons (Cordes & Lazio 2002) but uses other information such as parallax or HI absorption measurements if they are available. The uncertainty in the derived distances can exceed 50%, depending on

---

the pulsar. The table is sorted by decreasing $\sqrt{\dot{E}}/d^2$, assuming that $L_\gamma \propto V$ as discussed above. Such a ranking ignores effects of beam geometry relative to the Earth line-of-sight, and variations in L_γ that may stem from, for example, the angle between the neutron star's rotation and magnetic axes. Figure 1 shows $\sqrt{\dot{E}}/d^2$ normalized to Vela's value versus the rotation period for the gamma-ray pulsar candidates.

Table 1 also lists some pulsar wind nebulae (PWN) associated with young pulsars (Kaspi et al. 2004; Roberts 2004). Of the many striking results recently obtained from the HESS atmospheric Cherenkov imager array is the large number of Galactic sources in the TeV sky, most of which have been identified are PWN (see for example Aharonian et al. 2006). Table 1 gives TeV associations with HESS sources as well as a MILAGRO source (Abdo et al. 2007). Some of the unidentified EGRET sources are also likely to be PWN or pulsars. The table includes the angular distances to nearby EGRET 3rd catalog sources (Hartman et al. 1999). Many young pulsars are in or near the error boxes for these sources, and the LAT will better localize the GeV sources, making coincidence tests stronger. The pulsar timing campaign will enhance searches for GeV pulsations, to address whether the origin is in the neutron star magnetosphere or in the nebulae. One study aimed at distinguishing between true and fortuitous associations between young pulsars and their PWN or EGRET counterparts predicted that 19 ± 6 of the EGRET-pulsar associations will be confirmed by the GLAST LAT observations (Kramer et al. 2003).

The table further lists those rare pulsars seen beyond radio wavelengths, either in optical ("O" in the table), or in X-rays. The larger gamma-ray pulsar sample expected from the LAT will improve the current poor knowledge of the correlations between different types of high-energy emission.

Although we base the GLAST timing campaign on high $\dot{E}$ pulsars, we realize that pulsar gamma-ray emission is far from understood and therefore intend to study as many different pulsars as possible. The LAT's sensitivity and the continual sky-survey mode favor unexpected discoveries. The LAT team therefore welcomes long-term, phase-connected rotational ephemerides from astronomers wishing to collaborate on pulsed gamma-ray searches.

The main contributors to this timing campaign, by number of pulsars monitored, are the Parkes, Lovell (Jodrell Bank), and Nançay radio telescopes, "70 meter" class telescopes with high-performance pulsar backends. Jodrell Bank and Nançay provide redundant coverage of the northern sky. The Parkes telescope monitors pulsars south of $-10°$(and therefore shares some sources in common with the northern telescopes) and it is the only telescope in the campaign capable of observing sources below $-39°$. The Parkes telescope is described in Manchester et al. (2001) and the Lovell telescope pulsar performance is described in Morris et al. (2002). Theureau et al. (2005) describes the 2002 FORT upgrade to the Nançay receiver, with the new BON pulsar backend described in Cognard & Theureau (2006) and Camilo et al. (2007). The Urumqi radio observatory (Wang et al. 2001) is using a 25 meter antenna to monitor 38 of the brighter radio pulsars.

3.2. Timing Radio-Loud Gamma-Ray Candidates

The radio telescope time needed to monitor a given pulsar depends on the precision needed by the LAT, its radio flux density (e.g. S_{1400} in the ATNF catalog) and pulse profile, and the magnitude of its timing noise. Simple simulations indicate that gaus-
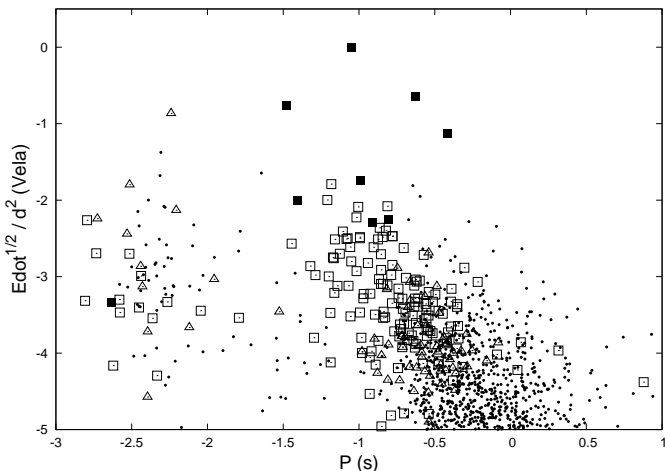
Fig. 1. $\sqrt{\dot{E}}/d^2$, normalized to Vela, versus neutron star rotation period. The pulsars with $\dot{E} > 3 \times 10^{34}$ erg/s (squares) and with 10^{34} erg/s $< \dot{E} < 3 \times 10^{34}$ erg/s (triangles) are those being timed regularly for the GLAST Large Area Telescope. The 9 solid squares correspond to the six confirmed EGRET pulsed detections and three pulsars for which there were indications of gamma pulsations. Dots: other pulsars. Pulsars in globular clusters are not plotted. We remind the reader that radio pulsars with high $\sqrt{\dot{E}}/d^2$ may nevertheless have gamma-ray beams directed away from the Earth line-of-sight and escape detection.

Fig. 2. Timing residuals for the 3.05 ms pulsar B1821−24, observed with the Nançay radio telescope. Crosses: 1.4 GHz, Squares: 2 GHz. Top: The observations at different frequencies were corrected using the same constant dispersion measure. Bottom: Same, with in addition a first-derivative of the dispersion measure to correct for the slope.

sian smearing of gamma-ray arrival times barely degrades detection sensitivity, for smearing widths up to 0.05 periods. Once detected, gamma photon statistics drive the need for higher precision: the timing residuals should be smaller than the phase histogram bin width, which in turn should be wide enough to have at least several gamma photons per bin. For gamma-faint pulsars, 0.05 periods is again a typical minimum requirement, increasing to the microsecond range for fast, gamma-bright pulsars.

A consequence of these relatively modest timing requirements is that a given radio observation need only last the minimum time for detection. More crucial is the number of observations per year, which depends on the timing noise, correlated with ν and $\dot{\nu}$ and thus $\dot{E}$ (Arzoumanian et al. 1994; Cordes & Helfand 1980). Gamma-ray candidates tend to be the noisiest pulsars. Illustrations of timing noise in young, high $\dot{E}$ pulsars can be found in Hobbs et al. (2006a). Glitches have been observed for roughly a quarter of the pulsars being monitored (Melatos et al. 2008). The bulk of the pulsars in this campaign are observed monthly, and a smaller number are observed weekly or bi-weekly.

The low radio fluxes of some gamma-ray pulsar candidates require long exposures on the biggest radio telescopes. Geminga illustrates the fact that the radio and gamma-ray intensities detected at any particular point in space are not necessarily correlated (Romani & Yadigaroglu 1995), suggesting (along with other evidence) that gamma-ray beams may be wider than the radio beams. We must therefore devote time to these radio-faint pulsars as they could be bright gamma-ray sources. Radio-faint, particularly noisy pulsars could dominate the observation schedules, as discussed in the next section.

Radio signals are dispersed by the interstellar medium, with a frequency dependent delay causing signals at high radio frequencies to arrive before those at low radio frequencies. The pulsar Dispersion Measure (DM), or the integrated column density of free electrons along the line of sight from a pulsar to Earth, allows extrapolation of the photon arrival times from radio to infinite frequency, as is required for gamma-ray studies. The DM,
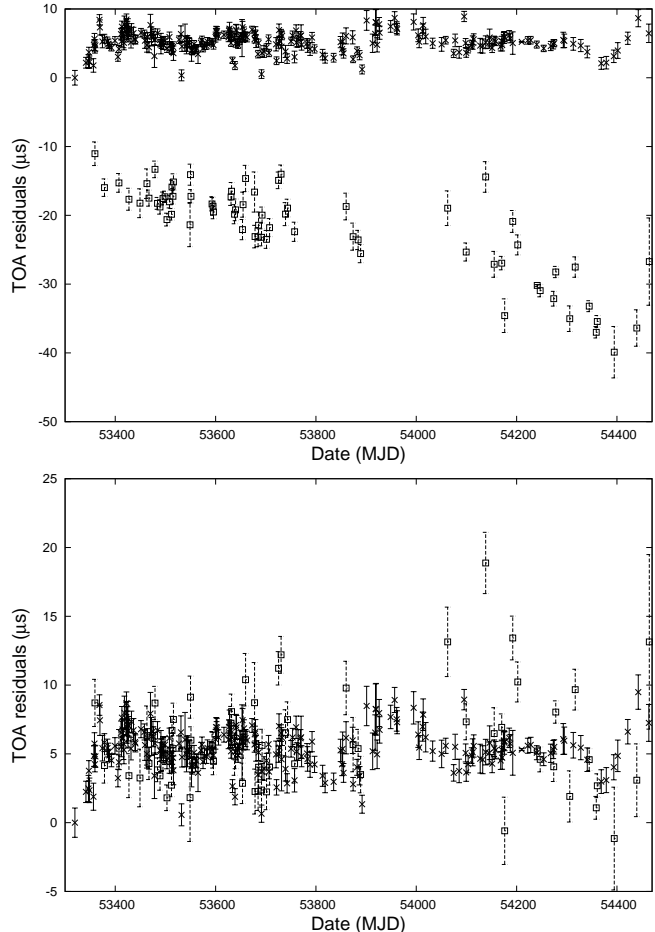
however, can change over timescales of weeks or years (You et al. 2007). If the DM is inaccurate, then the reference phase Φ_0 from the radio ephemeris (described below) will change, causing an apparent drift in the gamma-ray absolute phase and a smearing of the resulting gamma-ray pulse profiles. This will compromise the multi-wavelength phase comparisons upon which beam geometry studies are based. Therefore the timing campaign must include occasional monitoring at multiple radio frequencies. Figure 2 is one illustration of the magnitude of the dispersion for different radio frequencies. Figure 3 shows the potential effect of DM changes over time on a gamma-ray light curve. For the Crab pulsar, over several years, the maximum excursion in the photon time extrapolated from the radio frequency of 1400 MHz to infinite frequency is 0.3 ms (1% of a rotation of the neutron star). For pulsars faster than the Crab, the effect could be larger. For most pulsars, the effect is minor.

The radio pulsar monitoring must be sustained throughout the duration of the GLAST mission (i.e. for 5 to 10 years), a strain for any observatory, so other contributions are welcome. In particular, very frequent monitoring of high $\dot{E}$, large S_{1400} pulsars could allow significant contributions to LAT science by smaller radio telescopes.
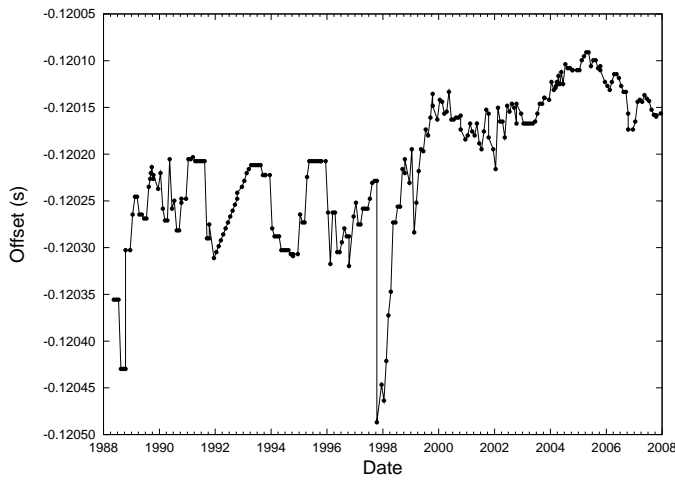
Fig. 3. Evolution of the dispersion measure (DM) correction of gamma-ray arrival times relative to the main radio peak, assuming a radio observation frequency 1400 MHz, for the Crab pulsar. The maximum excursion is 0.3 ms (0.01 in phase) over the years of the Compton GRO mission (1991-1999). Note: 120 ms ~ 4 Crab rotations. The DM values are from the Jodrell Bank monthly Crab ephemerides.

3.3. Radio-Quiet and Radio-Faint Pulsars

The archetypical radio-quiet gamma-ray pulsar is Geminga, PSR J0633+1746. Biannual XMM satellite measurements have ensured maintainance of a phase-coherent set of rotation parameters over the last few years (Jackson & Halpern 2005). The LAT will measure accurate light curves for Geminga in a few days and will maintain an accurate ephemeris through gamma-ray timing. The AGILE gamma-ray telescope has recently detected Geminga (A. Pellizzoni, private communication).

Table 1 includes 25 other pulsars (outside of globular clusters) with $S_{1400} < 0.1$ mJy, requiring long radio telescope integration times, if detectable at all. 10 of these have $\dot{E} > 10^{36}$ erg/s, making them both especially promising gamma-ray candidates, and subject to especially large timing noise.

Four high $\dot{E}$ pulsars are being timed with the Rossi X-ray Timing Explorer satellite (RXTE). PSR J1811−1925 was discovered in the center of the supernova remnant G11.2−0.3 in 1997 using the ASCA telescope (Torii et al. 1997). It has the highest $\sqrt{\dot{E}}/d^2$ of any radio-quiet pulsar after Geminga and we expect to detect it in gamma rays. It exhibits large timing noise. The young pulsar J1846−0258 resides in the core of a Crab-like pulsar wind nebula at the center of the bright shell-type SNR Kes 75. Based on its spin-down rate and X-ray spectrum, it is possibly the youngest known rotation-powered pulsar, with an estimated age of 884 yrs (Livingstone et al. 2006).

Two other young pulsars that may be bright GLAST sources are B0540−69 and J0537−6910 in the large Magellanic cloud. These pulsars have been monitored with RXTE over the last years and additional measurements in the first part of the GLAST mission are expected, before the end of the RXTE mission.

The remaining six high $\dot{E}$, low S_{1400} pulsars are J0205+6449, J1124−5916, J1747−2958, J1833−1034, J1930+1852, and J2021+3651. Depending on the pulse shape and the intensity of the surrounding radio nebulae, some of these are detectable with the 70-meter class telescopes. For the others, only the Arecibo and Green Bank (GBT) radio telescopes are appropriate.

GLAST will also perform "blind" searches for new radio-quiet pulsars (Ziegler et al. 2008), that is, search for pulsations in gamma-ray sources which are not known pulsars. Furthermore, the GLAST LAT may detect gamma-ray sources bearing neutron star signatures, for which no pulsations are observed, as was the case for the EGRET source 3EG J1835+5918 (Halpern et al. 2007; Reimer et al. 2001). The positional uncertainty obtained with the LAT should be small enough so that Arecibo, GBT and Parkes can perform deep radio pulsation searches.

4. GLAST LAT analysis software

4.1. The "Science Tools" and the ephemerides database

The GLAST LAT "Science Tools" provide a framework for analyzing gamma-ray data recorded by the Large Area Telescope: data subselection, exposure calculation, source detection and identification, likelihood analysis of emission spectra, etc. The "Science Tools" are developed and maintained by the GLAST Science Support Center [3]. This software is based on the standard *ftools* developed at HEASARC [4], designed for data sets using the FITS format. In this section we describe *gtbary* and *gtpphase*, which are pulsar timing analysis tools.

The pulsar section of the "Science Tools" allows basic timing analyses within the GSSC framework, but is *not* intended to replace specialized packages such as *TEMPO* (Taylor & Weisberg 1989) or *TEMPO2* (Hobbs et al. 2006b). The pulsar science tools include only a subset of the functions provided by the those packages.

We have tested *gtbary* and *gtpphase* with giant radio pulses from the Crab pulsar (B0531+21) and from the millisecond pulsar B1937+21, recorded at the Nançay radio telescope, X-ray photons from the binary millisecond pulsar J0218+4232 recorded by XMM, as well as with simulated radio observations of the binary millisecond pulsar J0437−4715 from Parkes.

Furthermore, we made extensive use of pulsar timing solutions (ephemerides) in the context of these tests, obtained by monitoring pulsars in radio or X-ray wavelengths. We converted pulsar ephemerides to fit the LAT format. In practice, these LAT format ephemerides will be gathered in a FITS file called "D4", which will be updated regularly and will be available on the GSSC data servers. The D4 file contains a subset of the many parameters that radio or X-ray pulsar astronomers are able to provide. Hence, we are creating a web-based interface to access the ephemeris files provided by the observing campaign and generate the D4 FITS file needed by the Science Tools.

Another task that this web-based tool addresses is the following: during the GLAST mission, when doing a long-term follow-up of a pulsar, one might have to use overlapping ephemerides, or choose between ephemerides valid on the same epoch. Those ephemerides could come from different observatories possibly using different analysis methods. As an example, the definition of the arbitrary time T_0 when the pulsar rotational phase equals zero, *i.e.* $\Phi(T_0) = 0$ can differ between observatories. To ensure phase continuity when using overlapping pulsar timing solutions, it is important to have the template profiles used to build the ephemerides. The web-based tool will keep track of these template profiles. In the following we describe the pulsar timing analysis using the LAT software, and the different tests used to validate this process.

---

[3] http://glast.gsfc.nasa.gov/ssc/

[4] http://heasarc.gsfc.nasa.gov/lheasoft/ftools/ftools_menu.html

4.2. Building light curves with LAT software

Topocentric photon arrival times recorded at the observatory at finite frequency have to be transfered to solar system barycenter (SSB) times at infinite frequency, mainly by correcting times for the motion of the earth and the observatory in the solar system frame. Then one folds the barycenter times, using the Taylor series expansion for $\Phi(t)$:

$$\Phi(t) = \Phi_0 + \sum_{i=0}^{i=N} \frac{f_i \times (t - T_0)^{i+1}}{(i+1)!}$$

where T_0 is the reference epoch of the pulsar ephemeris, f_i is the frequency derivative of order i, and Φ_0 is the absolute phase, an arbitrary pulsar phase at $t = T_0$.

We have tested both *barycenter* and *phase-folding* tools. The procedure is:

- Conversion of the arrival times from the observatory-specific format to the LAT time format: Mission Elapsed Time (MET) TT, which is the number of seconds since 2001 January 1 at 00:00 (UTC).
- Calculation of the orbital or ground-based observatory position, and conversion to the LAT spacecraft position format.
- Transfer of the topocentric times to the barycentric frame, using *"gtbary"*.
- Calculation of the pulsar phase for each arrival time, using *"gtpphase"*.

We have used real X-ray photon and giant radio pulse arrival times. X-ray and gamma-ray data are similar, since they are made up of "events" occuring at the random times when electronic thresholds are exceeded subsequent to an X-ray or gamma-ray arrival and interaction. Radio data are quite different: it is a periodic sampling of the voltage at the antenna backend. Giant radio pulses (GRPs) allow gamma-ray emulation with a radio telescope. In the following, X-ray photons and GRPs will be refered to as "events".

4.3. Simulated observations of an artificial pulsar

To test the barycenter software alone, we have simulated arrival times at Nançay observatory and compared LAT barycenter software with *TEMPO* and *TEMPO2*.

Some time and coordinate definition differences exist between these different codes. Most *TEMPO* pulsar timing solutions have been published using the JPL DE200 planetary ephemerides (Standish 1990). *TEMPO* forms barycentric times in "Barycentric Dynamic Time" (TDB). *TEMPO2* uses the JPL DE405 (Standish 1998) solar system ephemerides and computes barycentric time in "Barycentric Coordinate Time" (TCB) units, taking into account the time dilation results from Irwin & Fukushima (1999). The LAT barycenter tool *gtbary* handles both the DE200 ephemerides and the recommended JPL DE405 model, also forming TDB times. The relation between TDB and TCB times is given by:

$$TDB \simeq TCB - L_B \times \Delta T$$

where $L_B = 1.550519767 \times 10^{-8} \pm 2 \times 10^{-17}$ and $\Delta T = $ (date − 1977 January 1, 00:00) TAI ×86400 s. TAI times refer to "International Atomic Time". (*TEMPO2* has a *TEMPO* emulation mode, setting the barycentric time to TDB.) More details
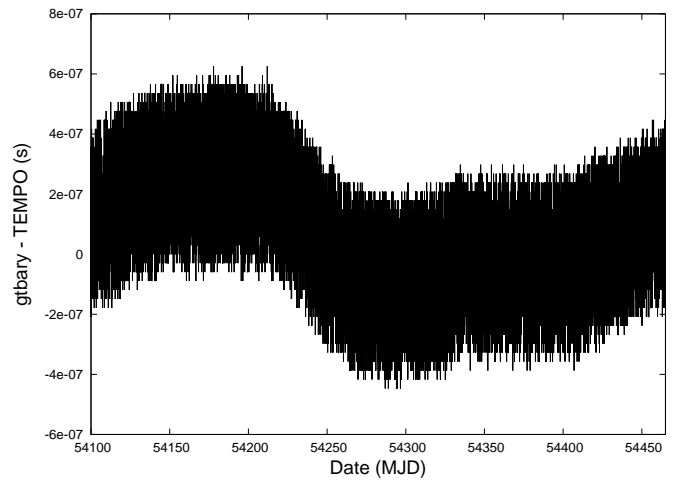

Fig. 4. *TEMPO-gtbary* comparison. *TEMPO2-gtbary* looks very similar.

on time-coordinate definitions can be found in Andersen (1999), Rickman (2001) and McCarthy & Petit (2004).

In the simulation, 10000 arrival times are recorded on the ground, beginning on MJD 54100 (arbitrary), with a constant step size (no assumption of periodic emission is made), over 1 year. Nançay times are expressed in Modified Julian Days (MJD) UTC, at finite frequency. They first have to be moved to the LAT time format, at infinite frequency. The dispersion delay in the propagation of a signal at a frequency at the solar system barycenter f_{SSB} through the interstellar medium is the following:

$$\Delta t = -\frac{DM}{K f_{SSB}^2}$$

where $K \equiv 2.410 \times 10^{-4}$ MHz^{-2} cm^{-3} pc s^{-1} is the *dispersion constant* (see e.g. Manchester & Taylor 1977) and *DM* is the *dispersion measure*. Note that the frequency at the barycenter f_{SSB} is different from the frequency at the observatory, due to the Doppler shift resulting from the motion of the observatory with respect to the pulsar (Edwards et al. 2006). Higher order relativistic corrections are neglected here. The simulated values for the pulsar position at J2000 epoch and dispersion measure are $(\alpha, \delta) = (20.75°, 45°)$, and $DM = 0$ cm^{-3} pc.

The position of the radio telescope with respect to the solar system barycenter for each time of arrival was calculated using the DE200 model in the *TEMPO-gtbary* comparison, and using the DE405 model with *TEMPO2* in TDB mode for the *TEMPO2-gtbary* comparison. The topocentric times are then transfered to the SSB. The resulting differences as a function of time are shown in Figure 4. In both cases, time differences are below 0.7 μs, better than the instrumental precision. We conclude that there is agreement between the LAT barycenter code and the other standard tools.

4.4. Giant radio pulses from the Crab pulsar, recorded at Nançay

Giant pulses are known only from a handful of energetic pulsars, including both young and millisecond pulsars, and occupy very small windows of pulsar phase (see e.g. Johnston & Romani 2004; Knight et al. 2006). Giant pulses from the Crab are bright and common. Between 22 March and 19 November 2007, Crab
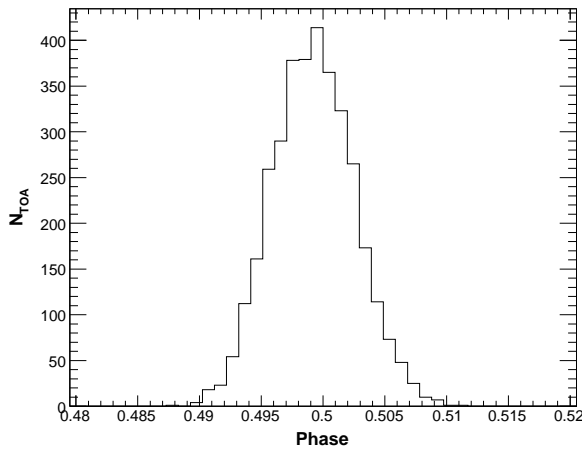
Fig. 5. Giant radio pulses from the Crab pulsar recorded at Nançay. The absolute phase is defined so that the main radio pulse is centered on 0.5.

GRPs were recorded with the Nançay radio telescope in 16 different frequency channels, from 1368 MHz to 1428 MHz. The acquisition of GRPs from the Crab pulsar at the Nançay observatory is described in Oosterbroek et al. (2008). Times of arrival for 3498 main component events with signal to noise ratio exceeding 20 standard deviations were recorded. Data were folded using contemporaneous Jodrell ephemerides (Lyne et al. 1993). All 9 monthly ephemerides used for this study had accuracy better than 160 μs. Again, times and observatory positions are converted to the LAT format. Event times are then converted to the barycenter and phase-folded using LAT software. The resulting phase histogram is shown in Figure 5. We found that the mean GRP arrival time is 32 μs before that predicted by the Jodrell Bank ephemerides, well within ephemeris accuracies. This is consistent with Shearer et al. (2003) results. Figure 5 demonstrates our ability to phase gamma-ray data over a long data span, even in the presence of significant timing noise. The codes are here validated at a few tens of μs level.

4.5. Giant radio pulses from B1937+21, recorded at Nançay

Giant pulses from B1937+21 were originally discovered and studied in detail by Cognard et al. (1996). A study by Kinkhabwala & Thorsett (2000) using the Princeton Mark IV instrument at the Arecibo telescope revealed that that giant pulses from B1937+21 occur in windows shorter than 10 μs, located 55 to 70 μs after the main radio pulse and interpulse. This is interesting for our tests since it allows more precise validation than giant pulses from the Crab pulsar.

Between 13 March and 7 April 2007, three measurements of giant pulses from the isolated millisecond pulsar B1937+21 were made at the Nançay radio telescope. Dates for 251 events with signal to noise exceeding 30 standard deviations were recorded. Again, the dispersion of radio waves by the interstellar medium is taken into account and times and observatory positions for each date are converted to the LAT format.

The timing solution used here was also derived from Nançay data. We use *gtbary* with the pulsar position corrected for proper motion, and *gtpphase* to calculate event phases. Figure 6 shows the resulting phases, along with a pulse profile at 1.4 GHz for B1937+21. The mean delays between the main and secondary giant pulse components and their regular emission counterparts
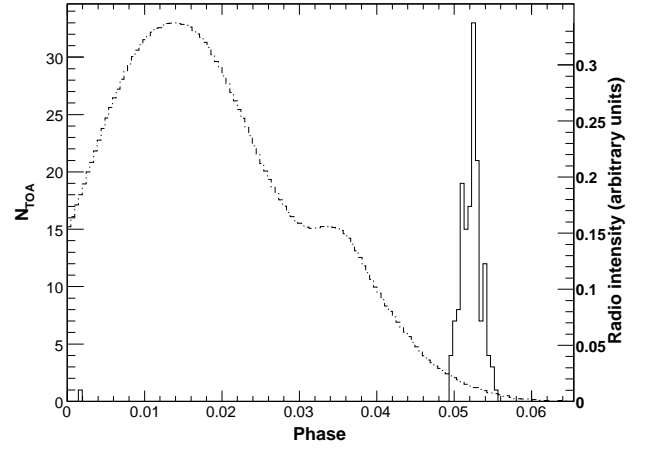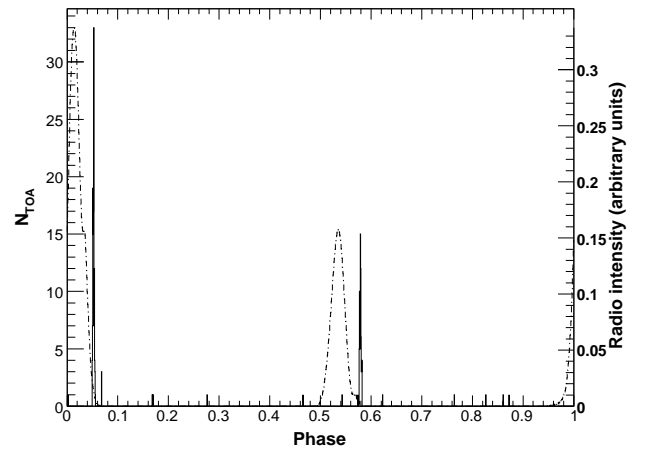
Fig. 6. Giant radio pulses from B1937+21 recorded at Nançay (solid line, left-hand scale), along with the template radio profile at 1.4 GHz used for this study (dashed line, right-hand scale). Top: whole phase histogram. Bottom: zoom on the main radio component.

are 60.1 and 67.3 μs respectively, with rms deviations of 1.9 and 2.4 μs, consistent with Kinkhabwala & Thorsett's results. We have thus validated both barycenter and phase-folding procedures, using events recorded on a three week timescale, for an isolated millisecond pulsar.

4.6. X-ray data from PSR J0218+4232, observed by XMM-Newton

Orbital movement has to be taken into account for pulsars in binary systems. The 2.3 millisecond pulsar J0218+4232 is in a binary system with a low mass white dwarf (Kuiper et al. 2002). It has been extensively studied at gamma-ray energies and is expected to be a bright GLAST source (Guillemot et al. 2007).

XMM-Newton, an X-ray satellite operating between 0.1 and 12 keV, made a 36 ks observation of J0218+4232 on 2002 February 11-12, with the PN camera[5]. In timing mode, this instrument has a timing resolution of 30 μs. Only events well calibrated in energy were retained. Pulsar data were collected using a rectangular region centered on the source. The back-

---

[5] We thank N. Webb (CESR - Toulouse) for providing us with the XMM-Newton data.

Fig. 8. Simulated times of arrival from the binary millisecond pulsar J0437−4715 recorded at Parkes. The absolute phase is defined so that the main radio pulse is centered on 0.5.

Fig. 7. X-ray photons from J0218+4232, recorded by the XMM-Newton satellite, between 1.6 and 4 keV. Black solid line: mean background level. Black dotted lines: peak positions in Webb et al. (2004), respectively $\Phi_1 = 0.24$ and $\Phi_2 = 0.73$.

ground level (shown in Figure 7) was estimated by selecting data from a similar region, in the same dataset, centered about 50" away from the pulsar, where no X-ray source could be detected. Finally, only events with energy between 1.6 and 4 keV were selected, to allow comparison with studies using the same dataset done by Webb et al. (2004).

Event times recorded by XMM-Newton are expressed in MET TT since 1998 January 1 at 00:00 (TT), and hence have to be converted to the LAT time format. As for the standard XMM-Newton analysis, satellite positions as a function of time were determined by a combination of Kepler orbital parameters and Chebyshev polynomials. Positions were interpolated to fit the GLAST position format.

Event times were converted to the barycenter, then corrected for the pulsar orbital motion and folded, based on radio ephemerides given in Kuiper et al. (2002). However, as in Webb et al. (2004) we tested frequencies around the nominal value with a χ^2 test, and found a shift in frequency of $\Delta \nu = 2.6 \times 10^{-6}$ Hz. The resulting phase histogram between 1.6 and 4 keV is shown in Figure 7. The peaks are centered on 0.26 and 0.74 respectively, which are within 40 μs of Webb et al's results.

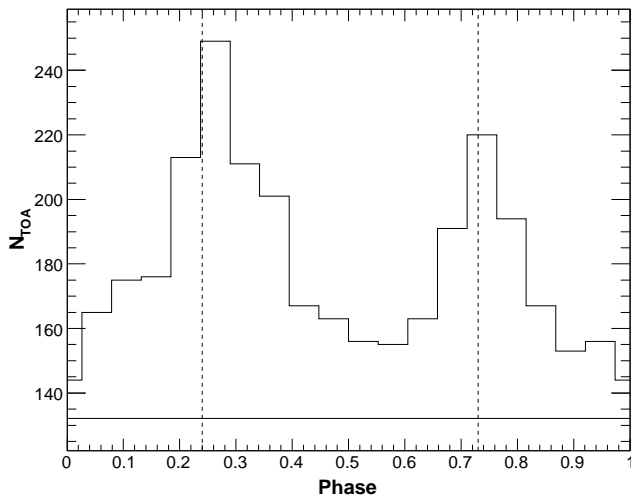### 4.7. Simulated radio data for PSR J0437−4715 observed with the Parkes telescope

The millisecond pulsar J0437−4715 has a pulse period of 5.76 ms, and is in a binary system with a 5.74 day orbital period. "Post-Keplerian" (PK) parameters, such as the rate of periastron advance, $\dot{\omega}$, or the rate of orbital period decay, $\dot{P}_b$, can be fit for this binary system (e.g. van Straten et al. 2001). A 500 day observation of J0437−4715 at the Parkes observatory was simulated using *TEMPO2* along with the *FAKE* plugin, resulting in 37 times of arrival.

For this simulation, a 199 ns accuracy timing solution for J0437−4715 derived from real Parkes observations made between April 1996 and March 2006 was used (Verbiest et al. 2008). For the analysis, we needed to convert the timing solution to a *gtpphase*-compatible version, with fewer orbital param-

eters than *TEMPO2* can handle. This was done using *TEMPO2*, leading to a timing solution with 292 ns.
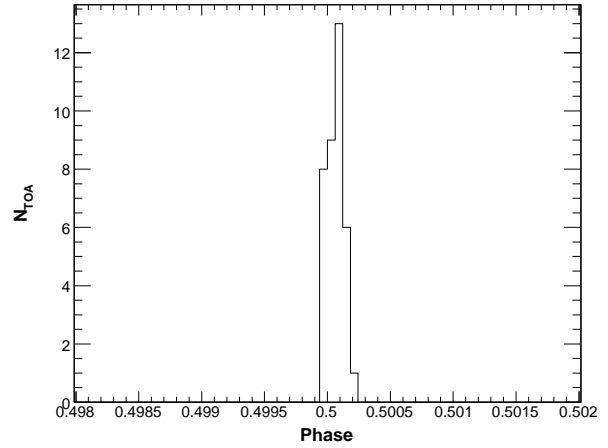
Event times were transfered to the solar system barycenter, having taken dispersion of radio waves and pulsar proper motion into account. Finally, times of arrival were phase-folded based on the *gtpphase*-compatible version of the J0437−4715 ephemeris. This led to the phase histogram given in Figure 8. The mean phase calculated with the LAT software is delayed from the *TEMPO2* mean value by 0.32 μs, resulting in a validation of the code below the μs level.

5. Prospects and Conclusions

We have motivated and described the large timing campaign that is underway in preparation for the GLAST mission. Previous campaigns resulted in a wealth of information on young pulsars, and we expect this effort will expand gamma-ray pulsar detections to middle-aged, older and millisecond pulsars as well. A large database of gamma-ray pulsars of many types will allow a study of trends and correlations in important properties such as gamma-ray flux, spectral index, profile shape and spectral cut-off. We further hope that the ephemeris database will be a useful tool for other instruments searching for pulsed emission at other photon energies, or in non-photon cosmic messengers, such as for example neutrinos. The individual observatories contributing to this campaign plan to publish the results of their timing campaign after GLAST has been in operation for some time.

References

Abdo, A. A., Allen, B., Berley, D., et al. 2007, ApJ, 664, 91
Aharonian, F., Akhperjanian, A. G., Bazer-Bachi, A. R., et al. 2006, A&A, 460, 365
Albert, J., Aliu, E., Anderhub, H., et al. 2008, ApJ, 674, 1037
Andersen, J. 1999, Transactions of the IAU, Series B, 23
Arons, J. 1996, A&AS, 120, 49

Arzoumanian, Z., Nice, D. J., Taylor, J. H., & Thorsett, S. E. 1994, ApJ, 422, 671

Atwood, W. B., Ziegler, M., Johnson, R. P., & Baughman, B. M. 2006, ApJ, 652, 49

Burderi, L., Fauci, F., & Boriakoff, V. 1999, ApJ, 512, 59

Camilo, F., Lorimer, D. R., Freire, P., Lyne, A. G., & Manchester, R. N. 2000, ApJ, 535, 975

Camilo, F., Cognard, I., Ransom, S. M., et al. 2007, ApJ, 663, 497

Cheng, K. S., Ho, C., & Ruderman, M. 1986a, ApJ, 300, 500

Cheng, K. S., Ho, C., & Ruderman, M. 1986b, ApJ, 300, 522

Chiang, J. & Romani, R. W. 1994, ApJ, 436, 754

Cognard, I., Shrauner, J. A., Taylor, J. H., & Thorsett, S. E. 1996, ApJ, 457, 81

Cognard, I. & Theureau, G. 2006, in "On the Present and Future of Pulsar Astronomy", 26th meeting of the IAU, 2, 36

Cordes, J. M. & Helfand, D. J. 1980, ApJ, 239, 640

Cordes, J. M. & Lazio, T. J. W. 2002, [arXiv:astro-ph/0207156]

D'Amico, N., Grueff, G., Montebugnoli, S., et al. 1996, ApJS, 106, 611

D'Amico, N., Lyne, A. G., Manchester, R. N., Possenti, A., & Camilo, F. 2001, ApJ, 548, 171

de Naurois, M., Holder, J., Bazer-Bachi, R., et al. 2002, ApJ, 566, 343

Edwards, R. T., Hobbs, G. B., & Manchester, R. N. 2006, MNRAS, 372, 1549

Gonthier, P. L., Ouellette, M. S., Berrier, J., O'Brien, S., & Harding, A. K. 2002, ApJ, 565, 482

Gonthier, P. L., Van Guilder, R., & Harding, A. K. 2004, ApJ, 604, 775

Guillemot, L., Lonjou, V., Dumora, D., et al. 2007, in AIP Conference Series, ed. S. Ritz, P. F. Michelson & C. A. Meegan, 921, 395

Halpern, J. P., Camilo, F., & Gotthelf, E. V. 2007, ApJ, 668, 1154

Harding, A. K. 2007, in AIP Conference Series, ed. S. Ritz, P. F. Michelson & C. A. Meegan, 921, 49

Harding, A. K., Grenier, I. A., & Gonthier, P. L. 2007, Ap&SS, 309, 221

Hartman, R. C., Bertsch, D. L., Bloom, S. D., et al. 1999, ApJS, 123, 79

Hobbs, G. B., Edwards, R. T., & Manchester, R. N. 2006a, MNRAS, 369, 655

Hobbs, G. B., Lyne, A. G., & Kramer, M. 2006b, Chinese Journal of Astronomy and Astrophysics Supplement, 6, 169

Irwin, A. W. & Fukushima, T. 1999, A&A, 348, 642

Jackson, M. S. & Halpern, J. P. 2005, ApJ, 633, 1114

Jacoby, B. A., Bailes, M., van Kerkwijk, M. H., et al. 2003, ApJ, 599, 99

Johnston, S., Manchester, R. N., Lyne, A. G., Kaspi, V. M., & D'Amico, N. 1995, A&A, 293, 795

Johnston, S. & Romani, R. W. 2004, in "Young Neutron Stars and Their Environments", IAU Symposium, ed. F. Camilo & B. M. Gaensler, 218, 315

Kaspi, V. M., Crawford, F., Manchester, R. N., et al. 1998, ApJ, 503, 161

Kaspi, V. M., Roberts, M. S. E., & Harding, A. K. 2004, in "Compact Stellar X-ray Sources", ed. W. H. G. Lewin & M. van der Klis, [arXiv:astro-ph/0402136]

Kinkhabwala, A. & Thorsett, S. E. 2000, ApJ, 535, 365

Knight, H. S., Bailes, M., Manchester, R. N., Ord, S. M., & Jacoby, B. A. 2006, ApJ, 640, 941

Kramer, M., Bell, J. F., Manchester, R. N., et al. 2003, MNRAS, 342, 1299

Kuiper, L., Hermsen, W., Verbunt, F., et al. 2002, ApJ, 577, 917

Kuiper, L., Hermsen, W., & Stappers, B. 2004, Adv. Space Res., 33, 507

Livingstone, M. A., Kaspi, V. M., Gotthelf, E. V., & Kuiper, L. 2006, ApJ, 647, 1286

Lorimer, D. R. & Kramer, M. 2004, Handbook of Pulsar Astronomy (Cambridge University Press)

Lyne, A. G., Pritchard, R. S., & Graham-Smith, F. 1993, MNRAS, 265, 1003, monthly Crab pulsar ephemerides are available at http://www.jb.man.ac.uk/pulsar/crab.html

Manchester, R. N., Lyne, A. G., Camilo, F., et al. 2001, MNRAS, 328, 17

Manchester, R. N. & Taylor, J. H. 1977, Pulsars (W. H. Freeman), 36

Manchester, R. N., Hobbs, G. B., Teoh, A., & Hobbs, M. 2005, AJ, 129, 1993

McCarthy, D. D. & Petit, G. 2004, IERS Conventions (International Earth Rotation and Reference Systems Service (IERS))

McLaughlin, M. A. & Cordes, J. M. 2000, ApJ, 538, 818

Melatos, A., Peralta, C., & Wyithe, J. S. B. 2008, ApJ, 672, 1103

Michelson, P. F. et al. 2008, ApJ, submitted

Morris, D. J., Hobbs, G., Lyne, A. G., et al. 2002, MNRAS, 335, 275

Nel, H. I., Arzoumanian, Z., Bailes, K. T. S., et al. 1996, A&AS, 120, 89

Oosterbroek, T., Cognard, I., & Golden, A. 2008, A&A, accepted

Pellizzoni, A., Chen, A., Conti, M., et al. 2004, Adv. Space Res., 33, 625

Ransom, S. M. 2007, in AIP Conference Series, ed. S. Ritz, P. F. Michelson & C. A. Meegan, 921, 54

Ray, P. S., Thorsett, S. E., Jenet, F. A., et al. 1996, ApJ, 470, 1103

Reimer, O., Brazier, K. T. S., Carramiñana, A., et al. 2001, MNRAS, 324, 772

Rickman, H. 2001, Transactions of the International Astronomical Union, Series B, 24

Roberts, M. S. E. 2004, The Pulsar Wind Nebula Catalog (March 2005 version), available at http://www.physics.mcgill.ca/~pulsar/pwncat.html

Romani, R. W. & Yadigaroglu, I.-A. 1995, ApJ, 438, 314

Ruderman, M. A. & Sutherland, P. G. 1975, ApJ, 196, 51

Shearer, A., Stappers, B., O'Connor, P., et al. 2003, Science, 301, 493

Smith, D. A., Grove, J. E., et al. 2008, in Preparation

Smith, D. A. & Thompson, D. J. 2008, in "Neutron stars and pulsars, 40 years after the discovery", ed. W. Becker, in Press

Standish, E. M. 1990, A&A, 233, 252

Standish, E. M. 1998, A&A, 336, 381

Sturrock, P. A. 1971, ApJ, 164, 529

Taylor, J. H. & Weisberg, J. M. 1989, ApJ, 345, 434

Theureau, G., Coudreau, N., Hallet, N., et al. 2005, A&A, 430, 373

Thompson, D. J., Bailes, M., Bertsch, D. L., et al. 1999, ApJ, 516, 297

Torii, K., Tsunemi, H., Dotani, T., & Mitsuda, K. 1997, ApJ, 489, 145

van Straten, W., Bailes, M., Britton, M., et al. 2001, Nature, 412, 158

Verbiest, J. P. W., Bailes, M., van Straten, W., et al. 2008, in Press, [arXiv:astro-ph/0801.2589]

Wagner, R. 2008, available at http://www.mpi-hd.mpg.de/hfm/HESS/public/HESS_catalog.htm

Wang, N., Manchester, R. N., Zhang, J., et al. 2001, MNRAS, 328, 855

Webb, N. A., Olive, J.-F., & Barret, D. 2004, A&A, 417, 181

You, X. P., Hobbs, G. B., Coles, W. A., et al. 2007, MNRAS, 378, 493

Ziegler, M., Baughman, B. M., Johnson, R. P., & Atwood, W. B. 2008, ApJ, accepted

PSR	PSRJ	$\frac{\sqrt{\dot{E}}}{d^2}$ % of Vela	$\dot{E}$ (erg/s)	d (kpc)	S_{1400} (mJy)	S_{400} (mJy)	Cluster, Galaxy	Optical X-ray	EGRET nearby	EgretDist (°)	TeV assoc.	Notes
B0833−45	J0835−4510	100.	6.9e+36	0.3	1100.	5000.		OX	3EG J0834−4511	0.34	Vela	G263.9−3.3, Vela X
J0633+1746	J0633+1746	22.	3.3e+34	0.2	—	—		OX	3EG J0633+1751	0.24		G195.1+4.3, Geminga
B0531+21	J0534+2200	17.	4.6e+38	2.0	14.	646.		OX	3EG J0534+2200	0.13	Crab	G184.6−5.8, Crab, SN1054
J0437−4715	J0437−4715	14.	1.2e+34	0.2	142.	550.		X				G253.4−42.0
B0656+14	J0659+1414	7.42	3.8e+34	0.3	3.70	6.50		OX				Monogem Ring
B0743−53	J0745−5353	5.37	1.1e+34	0.2	—	23.						
J0034−0534	J0034−0534	1.90	3.0e+34	0.5	0.61	17.						
J0205+6449	J0205+6449	1.62	2.7e+37	3.2	0.04	—		X				G130.7+3.1, 3C 58, SN1181
J0613−0200	J0613−0200	1.58	1.3e+34	0.5	1.40	21.						
J1747−2958	J1747−2958	1.25	2.5e+36	2.0	0.25	—			3EG J1744−3011 (*)	0.84	HESS J1745−303	G359.23−0.82, Mouse
B1706−44	J1709−4429	1.11	3.4e+36	2.3	7.30	25.		X	3EG J1710−4439	0.18		G343.1−2.3
B1055−52	J1057−5226	1.06	3.0e+34	0.7	—	80.		X	3EG J1058−5234	0.12		
J1833−1034	J1833−1034	1.00	3.4e+37	4.3	0.07	—					HESS J1833−105	G21.5−0.9
J1740+1000	J1740+1000	0.99	2.3e+35	1.2	9.20	3.10						
B1951+32	J1952+3252	0.98	3.7e+36	2.5	1.00	7.00						G69.0+2.7, CTB 80
J1357−6429	J1357−6429	0.90	3.1e+36	2.5	0.44	—		X				
B1509−58	J1513−5908	0.76	1.8e+37	4.2	0.94	1.50		X			HESS J1514−591	G320.4−1.2, MSH 15-52
B1257+12	J1300+1240	0.74	1.9e+34	0.8	2.00	20.		np				
J1524−5625	J1524−5625	0.73	3.2e+36	2.8	0.83	—						
J1531−5610	J1531−5610	0.69	9.1e+35	2.1	0.60	—						
B1046−58	J1048−5832	0.60	2.0e+36	2.7	6.50	—			3EG J1048−5840	0.14		G287.4+0.58
B0355+54	J0358+5413	0.56	4.5e+34	1.1	23.	46.						
J0940−5428	J0940−5428	0.50	1.9e+36	3.0	0.66	—						
J1930+1852	J1930+1852	0.44	1.2e+37	5.0	0.06	—		X	3EG J1928+1733	1.46		G54.1+0.3
B1259−63	J1302−6350	0.37	8.2e+35	2.8	1.70	—		np			HESS J1302−638	
J0834−4159	J0834−4159	0.36	9.9e+34	1.7	0.19	—						
J1909−3744	J1909−3744	0.36	2.2e+34	1.1	—	3.[a]						
B0906−49	J0908−4913	0.35	4.9e+35	2.5	10.	28.						G270.3−1.0
J1509−5850	J1509−5850	0.34	5.2e+35	2.6	0.15	—						
B1823−13	J1826−1334	0.34	2.8e+36	3.9	2.10	—		np	3EG J1826−1302 (*)	0.55	HESS J1825−137	G18.0−0.7
J1809−1917	J1809−1917	0.34	1.8e+36	3.5	2.50	—		np			HESS J1809−193	
J0538+2817	J0538+2817	0.32	4.9e+34	1.5	1.90	8.20		X				S147
J1811−1925	J1811−1925	0.32	6.4e+36	5.0	—	—		X			HESS J1809−193	G11.2−0.3, SN 386
J1420−6048	J1420−6048	0.31	1.0e+37	5.6	0.90	—		X	3EG J1420−6038	0.17	HESS J1420−607	G313.6+0.3, Kookaburra
B1800−21	J1803−2137	0.31	2.2e+36	3.9	7.60	23.		np			HESS J1804−216	
J1046+0304	J1046+0304	0.30	1.4e+34	1.1	0.30	—						
B0114+58	J0117+5914	0.30	2.2e+35	2.2	0.30	7.60						
J2229+6114	J2229+6114	0.28	2.2e+37	7.2	0.25	—		X	3EG J2227+6122	0.54		G106.6+3.1
J1718−3825	J1718−3825	0.28	1.2e+36	3.6	1.30	—			3EG J1714−3857	1.18	HESS J1718−385	
B1727−33	J1730−3350	0.27	1.2e+36	3.5	3.20	9.20			3EG J1734−3232	1.57		
B0740−28	J0742−2822	0.27	1.4e+35	2.1	15.	296.						
J1617−5055	J1617−5055	0.27	1.6e+37	6.8	0.5[b]	—		X			HESS J1616−508	
J1843−1113	J1843−1113	0.27	6.0e+34	1.7	0.10	—						
J2129−5721	J2129−5721	0.26	2.3e+34	1.4	1.40	14.						
J1124−5916	J1124−5916	0.26	1.2e+37	6.5	0.08	—		X				G292.0+1.8, MSH 11−54
J1846−0258	J1846−0258	0.25	8.1e+36	6.0	—	—		X			HESS J1846−029	G29.7−0.3, Kes 75
J1913+1011	J1913+1011	0.24	2.9e+36	4.8	0.50	—					HESS J1912+101	
J1911−1114	J1911−1114	0.23	1.2e+34	1.2	0.50	31.			3EG J1904−1124	1.96		
J2043+2740	J2043+2740	0.23	5.6e+34	1.8	—	15.[c]		X				
J0855−4644	J0855−4644	0.22	1.1e+36	3.9	0.20	—						
J0218+4232	J0218+4232	0.22	2.4e+35	2.7	0.90	35.		X	3EG J0222+4253	1.03		
J1739−3023	J1739−3023	0.20	3.0e+35	2.9	1.00	—			3EG J1744−3011 (*)	1.10		
J1831−0952	J1831−0952	0.20	1.1e+36	4.0	0.33	—						
B1957+20	J1959+2048	0.20	1.6e+35	2.5	0.40	20.		np				G59.2−4.7

continuing next page. . .

PSR	PSRJ	$\frac{\sqrt{\dot{E}}}{d^2}$ % of Vela	$\dot{E}$ (erg/s)	d (kpc)	S_{1400} (mJy)	S_{400} (mJy)	Cluster, Galaxy	Optical X-ray	EGRET nearby	EgretDist (°)	TeV assoc.	Notes
J1105−6107	J1105−6107	0.20	2.5e+36	5.0	0.75	—		np	3EG J1102−6103	0.86		MSH 11−62
B1821−24	J1824−2452	0.19	2.2e+36	4.9	0.18	40.	M28	X				
B1853+01	J1856+0113	0.19	4.3e+35	3.3	0.19	3.40			3EG J1856+0114	0.05		G34.7−0.4, W44, 3C 392
B1757−24	J1801−2451	0.18	2.6e+36	5.2	0.85	7.80		np	3EG J1800−2338	1.26		G5.27−0.9,G5.4-1.2?
B0611+22	J0614+2229	0.18	6.2e+35	2.1	2.20	29.			3EG J0617+2238	0.69		
B1719−37	J1722−3712	0.16	3.3e+34	1.9	3.20	25.						
J1835−1106	J1835−1106	0.16	1.8e+35	2.8	2.20	30.						
B0540+23	J0543+2329	0.15	4.1e+34	2.1	9.00	29.						
J1913+0904	J1913+0904	0.14	1.6e+35	3.0	0.07	—						
J0857−4424	J0857−4424	0.13	2.6e+34	1.9	0.88	12.						
J0729−1448	J0729−1448	0.13	2.8e+35	3.5	0.70	—						
B1737−30	J1740−3015	0.12	8.2e+34	2.7	6.40	25.			3EG J1744−3011 (*)	0.86		
J1928+1746	J1928+1746	0.11	1.6e+36	5.8	0.25	—			3EG J1928+1733	0.29		
J1015−5719	J1015−5719	0.11	8.3e+35	5.1	0.90	—			3EG J1014−5705	0.47		
B1830−08	J1833−0827	0.11	5.8e+35	4.7	3.60	—					HESS J1834−087	
J1837−0604	J1837−0604	0.11	2.0e+36	6.4	0.70	—			3EG J1837−0606 (*)	0.18		
J1740−5340A	J1740−5340A	0.10	1.4e+35	3.4	1.^{d}	—	NGC6397					
B1449−64	J1453−6413	0.10	1.9e+34	2.	14.	230.						
J1637−4642	J1637−4642	0.099	6.4e+35	5.1	0.78	—			3EG J1639−4702	0.55		
J0631+1036	J0631+1036	0.098	1.7e+35	3.7	0.80	1.50		X				
J1702−4310	J1702−4310	0.096	6.3e+35	5.1	0.72	—						
J1301−6305	J1301−6305	0.094	1.7e+36	6.7	0.46	—					HESS J1301−631	
J1828−1101	J1828−1101	0.092	1.6e+36	6.6	2.90	—						
B1620−26	J1623−2631	0.091	2.0e+34	2.2	1.60	15.	M4		3EG J1626−2519	1.35		
B1634−45	J1637−4553	0.087	7.5e+34	3.2	1.10	15.			3EG J1639−4702	1.17		
J1702−4128	J1702−4128	0.082	3.4e+35	4.8	1.10	—					HESS J1702−420	
J1705−3950	J1705−3950	0.081	7.4e+34	3.3	1.50	—						
J1016−5857	J1016−5857	0.080	2.6e+36	8.0	0.46	—			3EG J1013−5915 (*)	0.89		G284.3−1.8
J0901−4624	J0901−4624	0.080	4.0e+34	2.8	0.46	—						
B2334+61	J2337+6151	0.080	6.2e+34	3.1	1.40	10.		np				
B1317−53	J1320−5359	0.076	1.7e+34	2.3	—	18.			3EG J1316−5244	1.75		
J1841−0345	J1841−0345	0.073	2.7e+35	4.8	1.40	—			3EG J1837−0423	1.29		
J1830−0131	J1830−0131	0.069	2.3e+34	2.6	0.35	—						
J1119−6127	J1119−6127	0.068	2.3e+36	8.4	0.80	—		np				G292.2−0.5
J1549−4848	J1549−4848	0.068	2.3e+34	2.7	0.47	17.						
J1816−0755	J1816−0755	0.065	2.5e+34	2.8	0.17	—						
J1857+0143	J1857+0143	0.064	4.5e+35	5.8	0.74	—			3EG J1856+0114	0.63	HESS J1858+020	
B1001−47	J1003−4747	0.064	3.0e+34	2.9	—	6.00						
B1610−50	J1614−5048	0.064	1.6e+36	7.9	2.40	—						
B1828−11	J1830−1059	0.060	3.6e+34	3.2	1.40	2.10						
J1648−4611	J1648−4611	0.059	2.1e+35	5.0	0.58	—			3EG J1655−4554	1.68		
B1643−43	J1646−4346	0.057	3.6e+35	5.8	0.98	—						G341.2+0.9
J1906+0746	J1906+0746	0.057	2.7e+35	5.4	0.55	0.90						
B0136+57	J0139+5814	0.055	2.1e+34	2.9	4.60	28.						
J1738−2955	J1738−2955	0.050	3.7e+34	3.5	0.29	—			3EG J1736−2908 (*)	1.07		
B1730−37	J1733−3716	0.050	1.5e+34	2.8	3.40	—						
B0021−72F	J0024−7204F	0.049	1.4e+35	4.9	0.15^e	—	47Tuc					
J1723−3659	J1723−3659	0.049	3.8e+34	3.5	1.50	—						
J1715−3903	J1715−3903	0.049	6.9e+34	4.1	0.46	—			3EG J1714−3857	0.33		
J1601−5335	J1601−5335	0.048	1.0e+35	4.5	0.22	—						
J1514−5925	J1514−5925	0.048	3.5e+34	3.5	0.27	—					HESS J1514−591	
B1937+21	J1939+2134	0.048	1.1e+36	8.3	10.	240.		X				
B1820−30A	J1823−3021A	0.046	8.3e+35	7.9	0.72	16.	NGC6624					
J1828−1057	J1828−1057	0.046	5.5e+34	4.0	0.23	—						
J0905−5127	J0905−5127	0.045	2.4e+34	3.3	1.10	12.						
J1112−6103	J1112−6103	0.045	4.5e+36	12.2	1.40	—						

PSR	PSRJ	$\frac{\sqrt{\dot{E}}}{d^2}$ % of Vela	$\dot{E}$ (erg/s)	d (kpc)	S_{1400} (mJy)	S_{400} (mJy)	Cluster, Galaxy	Optical X-ray	EGRET nearby	EgretDist (°)	TeV assoc.	Notes
B1221−63	J1224−6407	0.044	1.9e+34	3.1	3.90	48.						
B1727−47	J1731−4744	0.042	1.1e+34	2.8	12.	190.						
B1356−60	J1359−6038	0.041	1.2e+35	5.2	7.60	105.						
J1921+0812	J1921+0812	0.040	2.3e+34	3.5	0.66	—						
B1915+13	J1917+1353	0.039	3.8e+34	4.0	1.90	43.						
B0021−72E	J0024−7204E	0.039	8.8e+34	4.9	0.21^e	—	47Tuc					
J1838−0549	J1838−0549	0.039	1.0e+35	5.1	0.29	—			3EG J1837−0606 (*)	0.50	HESS J1841−055	
J1548−5607	J1548−5607	0.039	8.5e+34	4.9	1.00	—						
J1835−0944	J1835−0944	0.039	5.6e+34	4.4	0.41	—						
J2021+3651	J2021+3651	0.038	3.4e+36	12.4	0.10	—		X	3EG J2021+3716 (*)	0.41	MGRO J2019+37	G75.2+0.1
B1535−56	J1539−5626	0.037	1.3e+34	3.1	4.60	—						
J1638−4608	J1638−4608	0.036	9.4e+34	5.2	0.33	—			3EG J1639−4702	0.91		
J1910−5959D	J1910−5959D	0.036	5.2e+34	4.5	0.05	—	NGC6752					
J1841−0524	J1841−0524	0.035	1.0e+35	5.3	0.20	—			3EG J1837−0606 (*)	1.39	HESS J1841−055	
J0024−7204O	J0024−7204O	0.033	6.5e+34	4.9	0.10^e	—	47Tuc					
B1754−24	J1757−2421	0.033	4.0e+34	4.4	3.90	20.			3EG J1800−2338	0.97		
J1452−5851	J1452−5851	0.032	3.5e+34	4.3	0.24	—						
J1541−5535	J1541−5535	0.032	1.1e+35	5.7	0.22	—						
J1643−4505	J1643−4505	0.031	9.4e+34	5.6	0.28	—						
B1607−52	J1611−5209	0.031	3.4e+34	4.3	1.20	—						
B1338−62	J1341−6220	0.030	1.4e+36	11.1	1.90	—		X				G308.8−0.1
J1907+0918	J1907+0918	0.029	3.2e+35	7.8	0.29	0.40						
J1016−5819	J1016−5819	0.029	4.1e+34	4.7	0.31	—			3EG J1013−5915 (*)	1.23		
J0537−6910	J0537−6910	0.029	4.9e+38	49.4	—	—	LMC	X	3EG J0533−6916	1.20		G279.6−31.7, N 157B
B1930+22	J1932+2220	0.028	7.5e+35	9.8	1.20	7.80						
J1853−0004	J1853−0004	0.028	2.1e+35	7.2	0.87	—			3EG J1856+0114	1.46		
J0024−7204U	J0024−7204U	0.028	4.6e+34	4.9	0.06^e	—	47Tuc					
J1019−5749	J1019−5749	0.028	1.8e+35	6.9	0.80	—			3EG J1014−5705 (*)	1.64		
B1556−57	J1600−5751	0.027	1.1e+34	3.5	1.40	20.						
J1841+0130	J1841+0130	0.027	1.2e+34	3.6	0.06	—						
J1543−5459	J1543−5459	0.026	3.8e+34	4.8	0.62	—						
J0954−5430	J0954−5430	0.026	1.6e+34	3.9	0.36	—						
J1737−3137	J1737−3137	0.026	6.0e+34	5.5	0.80	—			3EG J1734−3232	1.19		
J1650−4921	J1650−4921	0.025	1.9e+34	4.1	0.16	—						
J1815−1738	J1815−1738	0.025	3.9e+35	8.8	0.25	—					HESS J1813−178	
B1822−14	J1825−1446	0.025	4.1e+34	5.1	2.60	—			3EG J1824−1514 (*)	0.52	HESS J1826−148	
B1821−19	J1824−1945	0.024	3.0e+34	4.7	4.90	71.						
J1853+0056	J1853+0056	0.024	4.0e+34	5.1	0.21	—			3EG J1856+0114	0.68		
J1115−6052	J1115−6052	0.023	1.6e+34	4.1	0.38	—						
J1903+0925	J1903+0925	0.023	3.2e+34	4.9	0.20	—						
J1413−6141	J1413−6141	0.023	5.6e+35	10.1	0.61	—			3EG J1410−6147	0.80		
J1756−2225	J1756−2225	0.023	3.1e+34	5.0	0.25	—			3EG J1800−2338	1.50		
J1406−6121	J1406−6121	0.022	2.2e+35	8.2	0.36	—			3EG J1410−6147	0.90		
J0024−7204T	J0024−7204T	0.021	2.7e+34	4.9	—	—	47Tuc					
B1718−35	J1721−3532	0.021	4.5e+34	5.6	11.	—						
B1508−57	J1512−5759	0.021	1.3e+35	7.3	6.00	—						
B1832−06	J1835−0643	0.019	5.6e+34	6.2	1.30	—			3EG J1837−0606	0.78		
B1838−04	J1841−0425	0.019	3.9e+34	5.7	2.60	2.60			3EG J1837−0423 (*)	1.02		
J1538−5551	J1538−5551	0.019	1.1e+35	7.5	0.25	—						
J0024−7204Q	J0024−7204Q	0.018	2.0e+34	4.9	0.05^e	—	47Tuc					
J1138−6207	J1138−6207	0.018	3.0e+35	9.7	0.49	—						
J1156−5707	J1156−5707	0.018	4.3e+34	6.0	0.19	—						
J1734−3333	J1734−3333	0.018	5.6e+34	6.5	0.50	—			3EG J1734−3232	1.03		
J1412−6145	J1412−6145	0.018	1.2e+35	7.8	0.47	—			3EG J1410−6147	0.53		
J1743−3153	J1743−3153	0.017	5.8e+34	6.6	0.50	—			3EG J1744−3011	1.71		
J1632−4757	J1632−4757	0.017	5.0e+34	6.4	0.30	—			3EG J1639−4702	1.92	HESS J1632−478	

PSR	PSRJ	$\frac{\sqrt{\dot{E}}}{d^2}$ % of Vela	$\dot{E}$ (erg/s)	d (kpc)	S_{1400} (mJy)	S_{400} (mJy)	Cluster, Galaxy	Optical X-ray	EGRET nearby	EgretDist (°)	TeV assoc.	Notes
J1123−6259	J1123−6259	0.017	1.0e+34	4.3	0.56	11.						
J1909+0912	J1909+0912	0.017	1.3e+35	8.2	0.35	—						
J1650−4502	J1650−4502	0.017	1.1e+34	4.4	0.35	—			3EG J1655−4554	1.41		
J1638−4417	J1638−4417	0.016	3.9e+34	6.2	0.21	—						
B0540−69	J0540−6919	0.016	1.5e+38	49.4	0.02	—	LMC	OX	3EG J0533−6916	1.80		G279.7−31.5, N158A
J1834−0731	J1834−0731	0.015	1.7e+34	5.1	1.00	—			3EG J1837−0606	1.57		
J1052−5954	J1052−5954	0.015	1.3e+35	8.5	0.15	—			3EG J1048−5840	1.70		
B2148+52	J2150+5247	0.015	1.1e+34	4.6	2.00	16.						
J1649−4653	J1649−4653	0.015	1.1e+34	4.7	0.31	—			3EG J1655−4554	1.71		
J1551−5310	J1551−5310	0.015	8.3e+34	7.8	0.54	—						
J1843−0702	J1843−0702	0.015	1.2e+34	4.8	0.17	—			3EG J1837−0606	1.85		
J1907+0919	J1907+0919	0.014	2.2e+34	5.8	—	—						
J1349−6130	J1349−6130	0.014	1.2e+34	5.0	0.58	—						
J1913+0832	J1913+0832	0.014	7.4e+34	7.9	0.60	—						
J1838−0453	J1838−0453	0.013	8.3e+34	8.1	0.33	—			3EG J1837−0423 (*)	0.59		
J1627−4706	J1627−4706	0.013	2.5e+34	6.1	0.10	—						
J1837−0559	J1837−0559	0.013	1.6e+34	5.4	0.50	—			3EG J1837−0606 (*)	0.15	HESS J1841−055	
J1248−6344	J1248−6344	0.013	8.6e+34	8.3	0.12	—						
J1845−0743	J1845−0743	0.013	1.3e+34	5.2	2.70	—						
J1839−0905	J1839−0905	0.012	1.4e+34	5.4	0.16	—						
J1845−0316	J1845−0316	0.012	3.9e+34	7.0	0.35	—					HESS J1846−029	
J1801−2154	J1801−2154	0.012	1.2e+34	5.3	0.18	—			3EG J1800−2338	1.75		
J1853+0545	J1853+0545	0.012	1.2e+34	5.3	1.60	—						
J1907+0731	J1907+0731	0.011	1.5e+34	5.7	0.35	—						
B1557−50	J1600−5044	0.011	2.8e+34	6.7	17.	—						
J1755−2534	J1755−2534	0.011	3.5e+34	7.1	0.17	—						
J1452−6036	J1452−6036	0.011	1.5e+34	5.8	1.40	—						
J1839−0321	J1839−0321	0.011	3.6e+34	7.2	0.27	—			3EG J1837−0423	1.22		
J1632−4818	J1632−4818	0.011	4.8e+34	7.8	0.39	—					HESS J1632−478	
B1841−05	J1844−0538	0.011	2.3e+34	6.6	2.20	—			3EG J1837−0606	1.83		
J1550−5418	J1550−5418	0.011	1.0e+35	9.6	3.30	—						
B2000+32	J2002+3217	0.010	1.2e+34	5.7	1.20	5.50						
J1907+0345	J1907+0345	0.0094	2.3e+34	7.2	0.17	—						
J1842−0905	J1842−0905	0.0091	1.0e+34	5.9	0.81	—						
J1946+2611	J1946+2611	0.0089	1.1e+34	6.1	—	1.50						
J1726−3530	J1726−3530	0.0084	3.5e+34	8.4	0.30	—						
B1636−47	J1640−4715	0.0083	1.2e+34	6.5	1.20	—			3EG J1639−4702	0.38		
J1904+0800	J1904+0800	0.0082	3.7e+34	8.6	0.36	—						
J1820−1529	J1820−1529	0.0080	4.0e+34	8.9	0.61	—			3EG J1824−1514	0.87		
B2011+38	J2013+3845	0.0076	2.9e+34	8.4	6.40	26.			3EG J2016+3657	1.95		
J1908+0909	J1908+0909	0.0075	3.6e+34	9.0	0.22	—						
B1855+02	J1857+0212	0.0074	2.2e+34	8.0	1.60	—			3EG J1856+0114	1.07	HESS J1858+020	
J1903+0601	J1903+0601	0.0073	1.5e+34	7.2	0.26	—			3EG J1903+0550	0.21		
J1515−5720	J1515−5720	0.0072	1.0e+34	6.6	0.20	—						
J1853+0011	J1853+0011	0.0070	2.1e+34	8.1	0.30	—			3EG J1856+0114	1.21		
J1342+2822B	J1342+2822B	0.0068	5.4e+34	10.4	0.01	—	M3					
J1806−2125	J1806−2125	0.0068	4.3e+34	9.8	1.10	—						
J1626−4807	J1626−4807	0.0066	2.7e+34	8.9	0.37	—						
J1020−6026	J1020−6026	0.0065	9.6e+34	12.3	0.14	—						
J1305−6203	J1305−6203	0.0055	1.6e+34	8.5	0.62	—			3EG J1308−6112	1.08		
J1843−0355	J1843−0355	0.0055	1.8e+34	8.8	0.80	—			3EG J1837−0423	1.59		
J1735−3258	J1735−3258	0.0054	2.4e+34	9.6	0.46	—			3EG J1734−3232	0.66		
B2127+11E	J2129+1210E	0.0050	7.0e+34	12.9	—	0.20	M15					
B1758−23	J1801−2304	0.0050	6.2e+34	12.6	2.20	—			3EG J1800−2338 (*)	0.65		
J1043−6116	J1043−6116	0.0046	1.7e+34	9.5	0.91	—						
J1908+0839	J1908+0839	0.0045	1.5e+34	9.3	0.49	—						

PSR	PSRJ	$\frac{\sqrt{\dot{E}}}{d^2}$ % of Vela	$\dot{E}$ (erg/s)	d (kpc)	S_{1400} (mJy)	S_{400} (mJy)	Cluster, Galaxy	Optical X-ray	EGRET nearby	EgretDist (°)	TeV assoc.	Notes
J1808−2024	J1808−2024	0.0041	5.0e+34	13.1	—	—						
J1812−1910	J1812−1910	0.0035	1.9e+34	11.2	0.22	—						
J1327−6400	J1327−6400	0.0031	5.6e+34	15.5	0.36	—						
B2127+11F	J2129+1210F	0.0026	1.9e+34	12.9	—	0.10	M15					
J1524−5706	J1524−5706	0.0024	1.0e+34	11.4	0.41	—						
J1216−6223	J1216−6223	0.0013	1.3e+34	16.6	0.15	—						
J0535−6935	J0535−6935	0.00031	5.6e+34	49.4	0.05	—	LMC		3EG J0533−6916	0.59		
B0456−69	J0455−6951	0.00014	1.2e+34	49.4	—	0.60	LMC					

Table 1. Pulsars being timed for the GLAST Large Area Telescope (all known pulsars with $\dot{E} > 10^{34}$ ergs/s), ordered by $\sqrt{\dot{E}}/d^2$, where $\dot{E}$ is the spin-down energy loss rate and d is the distance. $\sqrt{\dot{E}}/d^2$ as an indicator of expected gamma flux suffers many large uncertainties (see text). S_{1400} and S_{400} are the radio flux densities at 1400 MHz and 400 MHz, respectively. "Cluster, Galaxy" is the name of the globular cluster or the host galaxy, if the pulsar is in one. "np" means that the source is observed in X-rays, but not pulsed. If the pulsar is located less than 2° away from a 3rd EGRET catalog source (Hartman et al. 1999), the EGRET name and the angular distance are listed. The asterisk (*) indicates that the 3EG source has more than one possible counterpart in the table. The TeV associations are taken from Wagner (2008), available at http://www.mpi-hd.mpg.de/hfm/HESS/public/HESS_catalog.htm, and from MILAGRO (Abdo et al. 2007). Nearby pulsar wind nebulae (PWN) are noted in the last column (Kaspi et al. 2004; Roberts 2004). The data in the first 8 columns were obtained from the ATNF database except for the radio flux densities with the superscripts *a*: Jacoby et al. (2003), *b*: Kaspi et al. (1998), *c*: Ray et al. (1996), *d*: D'Amico et al. (2001), *e*: Camilo et al. (2000). An electronic version of this table is posted at https://confluence.slac.stanford.edu/display/GLAMCOG/Pulsars+being+timed .